Boise State University
ScholarWorks

Materials Science and Engineering Faculty Publications and Presentations

Department of Materials Science and Engineering

8-1-2019

Oxidation Behavior of Zirconium, Zircaloy-3, Zircaloy-4, Zr-1Nb, and Zr- 2.5Nb in Air and Oxygen

Jordan L. Vandegrift
Boise State University

Patrick M. Price
Boise State University

John-Paul Stroud
Boise State University

Clemente J. Parga
Idaho National Laboratory

Isabella J. Van Rooyen
Idaho National Laboratory

See next page for additional authors

Publication Information

Vandegrift, Jordan L.; Price, Patrick M.; Stroud, John-Paul; Parga, Clemente J.; Van Rooyen, Isabella J.; Jaques, Brian J.; and Butt, Darryl P. (2019). "Oxidation Behavior of Zirconium, Zircaloy-3, Zircaloy-4, Zr-1Nb, and Zr- 2.5Nb in Air and Oxygen". *Nuclear Materials and Energy, 20*, 100692-1 - 100692-9. http://dx.doi.org/10.1016/j.nme.2019.100692

Authors
Jordan L. Vandegrift, Patrick M. Price, John-Paul Stroud, Clemente J. Parga, Isabella J. Van Rooyen, Brian J. Jaques, and Darryl P. Butt

This article is available at ScholarWorks: https://scholarworks.boisestate.edu/mse_facpubs/395

Nuclear Materials and Energy 20 (2019) 100692

Contents lists available at ScienceDirect

Nuclear Materials and Energy

journal homepage: www.elsevier.com/locate/nme

Oxidation behavior of Zirconium, Zircaloy-3, Zircaloy-4, Zr-1Nb, and Zr-2.5Nb in air and oxygen

Jordan L. Vandegrift[a,b,*], Patrick M. Price[a,b,c], John-Paul Stroud[a,b], Clemente J. Parga[d], Isabella J. Van Rooyen[d], Brian J. Jaques[a,b], Darryl P. Butt[a,b,e]

[a] Boise State University, 1910 University Dr, Boise, ID 83725, United States
[b] Center for Advanced Energy Studies, 995 University Blvd, Idaho Falls, ID 83401, United States
[c] Sandia National Laboratory, 1515 Eubank Blvd SE, Albuquerque, NM 87123, United States
[d] Idaho National Laboratory, 2525 Fremont Ave, Idaho Falls, ID 83402, United States
[e] University of Utah, 201 Presidents Cir, Salt Lake City, UT 84112, United States

ARTICLE INFO

Keywords:
Zirconium alloys
Breakaway
Oxidation
Thermogravimetric analysis

ABSTRACT

The Transient Reactor Test (TREAT) facility at the Idaho National Laboratory currently utilizes a legacy Zircaloy-3 cladding, which is no longer commercially available. TREAT is air cooled and routinely operates at temperatures well above that of traditional reactor designs. This study investigates the oxidation behavior of pure zirconium and its alloys (Zircaloy-3, Zircaloy-4, Zr-1Nb, Zr-2.5Nb) in Ar + 20%O_2 and N_2 + 20%O_2 atmospheres at temperatures ranging from 400–800 °C to determine which alloy should be implemented as TREAT's cladding. While the oxidation behavior of zirconium based cladding materials has been extensively documented, this study focuses on direct comparison between legacy Zircaloy-3 and contemporary alloys using a flat plate geometry and similar conditions seen at the TREAT facility. In this work, thermogravimetric analysis was used to measure both steady state and breakaway oxidation, which was then used to calculate oxidation rate constants and activation energies of each material. Oxide thickness was evaluated through microscopy of oxidized specimen cross sections. The Zircaloy-3 and Zr-1Nb alloys were found to be the most resistant to oxidation under the conditions of this study, whereas the Zr-2.5Nb alloy was found to be the most susceptible.

1. Introduction

The Transient Reactor Test (TREAT) facility, located at the Idaho National Laboratory (INL), is designed to provide safety data on various fuel designs during simulated transients varying between mild upsets to severe accidents. TREAT was decommissioned in 1994; however, it was reinstated to operational status in November of 2017. The core is being converted from a highly enriched uranium (HEU) core to a low enriched uranium (LEU) core, thus the structural materials used in the original core are being re-evaluated. TREAT's maximum operating temperature is limited by the rapid oxidation of the zirconium alloy cladding at high temperatures in air [1]. Due to this restriction, TREAT is designed such that the fuel core (including the zircaloy cladding) does not exceed a maximum temperature of 600 °C in normal transients with a design basis accident limit of 820 °C. Additionally, TREAT is air cooled. Nitrogen present in air has been shown by previous work to act as a catalyst for the oxidation reaction, resulting in faster oxidation kinetics and the formation of a more porous oxide when compared to oxidation in pure oxygen or steam [2–8]. Once the oxide reaches a critical thickness it cracks, creating a direct pathway for oxygen to reach the metal surface resulting in a transition from parabolic to faster oxidation kinetics [9]. This transition is termed “breakaway”. The resulting oxide is porous and cracked, compromising the mechanical stability of the cladding.

It is fairly well documented that the pre-breakaway regime during zircaloy oxidation is a diffusion limited process (controlled by the diffusion of oxygen anions) during which a dense oxide layer is formed [10–13]. The post-breakaway regime is controlled by the nucleation and growth of nodules at the metal/oxide interface. In the breakaway regime during corrosion in air, it is thought that three reactions take place: (1) Cracks begin to form in the dense ZrO_2 layer and ZrN and ZrO_2 form at the metal oxide interface, (2) ZrN is oxidized and the volume change results in cracks in ZrO_2, (3) nitrogen can become trapped between ZrO_2 and α-Zr(O) and form ZrN, which is then oxidized resulting in further cracking and oxidation [10,11,13].

While some research has been reported on the characterization of

* Corresponding author at: Boise State University, 1910 University Dr, Boise, ID 83725, United States.
E-mail address: jordanvandegrift@u.boisestate.edu (J.L. Vandegrift).

https://doi.org/10.1016/j.nme.2019.100692
Received 24 January 2019; Received in revised form 30 May 2019; Accepted 11 June 2019
Available online 12 June 2019
2352-1791/ © 2019 The Authors. Published by Elsevier Ltd. This is an open access article under the CC BY-NC-ND license (http://creativecommons.org/licenses/BY-NC-ND/4.0/).

Table 1
Composition (wt%) of zirconium alloys presented here. Zry-3, Zry-4, and Zr-1Nb are typical compositions for these alloys [9]. The composition from Zr-2.5Nb was provided by the manufacturing company.

	Sn	Fe	Cr	O	Nb	$H \times W \times T$ (mm)
Zry-3	0.25	0.25	–	–	–	10.1 × 7.5 × 0.63
Zry-4	1.2–1.7	0.18–0.24	0.07–0.13	0.1–0.14	–	10.1 × 7.5 × 1.62
Zr-1Nb	–	0.015–0.06	–	0.09–0.12	1	10.1 × 7.5 × 0.36
Zr-2.5Nb	–	610 (ppm)	–	1060 (ppm)	2.62	9.3 × 4.4 × 1.49

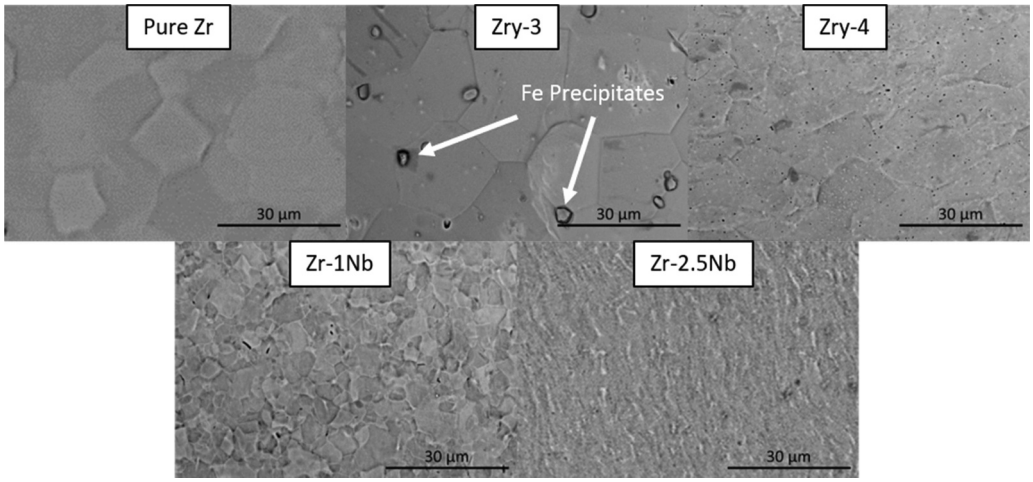

Fig. 1. Backscatter SEM images of the as received microstructure of the materials investigated.

the oxidation behavior of zirconium alloys under similar conditions, no publications were found that directly compare Zry-3, Zry-4, Zr-1Nb, Zr-2.5Nb, and Zr with similar geometry under similar conditions in the temperature range of interest to TREAT (400–800 °C). Duriez et al. provides direct comparisons of oxidized Zry-4 and M5® tube samples in air at temperatures between 600–1200 °C [2,3,14]. Their results conclude that the oxidation kinetics in Zry-4 are faster than in M5® both before and after breakaway oxidation when tested under the same experimental conditions with similar sample geometries. Steinbrük et al. investigated isothermal and non-isothermal oxidation of Zry-4 tubes in oxygen, air, and nitrogen from 800–1480 °C using thermogravimetric analysis (TGA) [6]. They found that Zry-4 tubes exhibit faster oxidation kinetics in air than in pure oxygen or nitrogen. Additionally, breakaway occurred earlier in samples oxidized in air and the resulting oxide was more porous. The authors attribute the increased oxidation behavior to the formation and subsequent re-oxidation of ZrN.

The work demonstrated here provides a direct comparison of the oxidation behavior of Zry-3, Zry-4, Zr-1Nb, Zr-2.5Nb, and pure zirconium with similar geometry and experimental conditions which will bridge discrepancies present in current literature. The results from the separate effects testing provide insight into the effect of nitrogen on the oxidation behavior of these zirconium-based alloys. The onset of breakaway oxidation and kinetics before and after breakaway are determined and the performance of the cladding materials is compared.

2. Experimental procedures

2.1. Specimens

The composition of the zirconium alloys used are shown below in Table 1. Additionally, scanning electron microscope (SEM) images of the microstructure of the as received materials are shown in Fig. 1. The Fe-rich precipitates found in Zry-3 are seen in the figure, however no precipitates were found in the other materials. The impurities present in the pure Zr are listed by the vendor (Goodfellow) in parts per million by mass as: Hf-(2500), O-(1000), C-(250), Fe-(200), Cr-(200), N-(100), H-(10). The materials were received in sheets of varying thickness (T) as listed in Table 1. The thickness of the pure Zr was 0.5 mm. Prior to oxidation, samples were machined from the sheets using electronic discharge machining (EDM). Zry-3, Zry-4, Zr-1Nb, and Zr had the dimensions 10.1 × 7.5 mm and Zr-2.5Nb had the dimensions 9.3 × 4.4 mm (due to the size of the original sheet of material received). Before oxidation experiments, the native oxide present on the samples was removed on all six surfaces by grinding with 800 and 1200 grit SiC paper. The samples were then sonicated in a 1:1:1 solution of acetone:ethanol:DI water and dried before loading into the simultaneous thermal analyzer (STA).

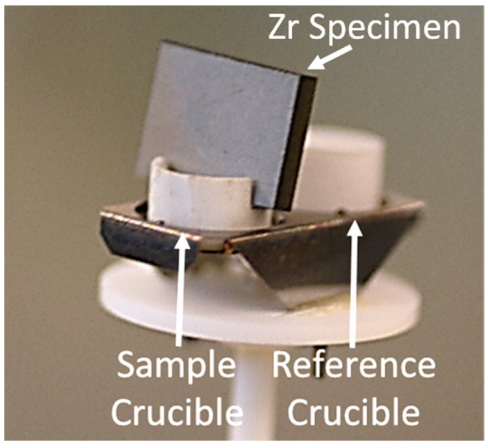

Fig. 2. Image showing the custom sample setup for the TGA. The platinum sample carrier is loaded with a notched alumina crucible to minimize contact between the sample and crucible while maximizing the surface area exposed to the oxidizing gas.

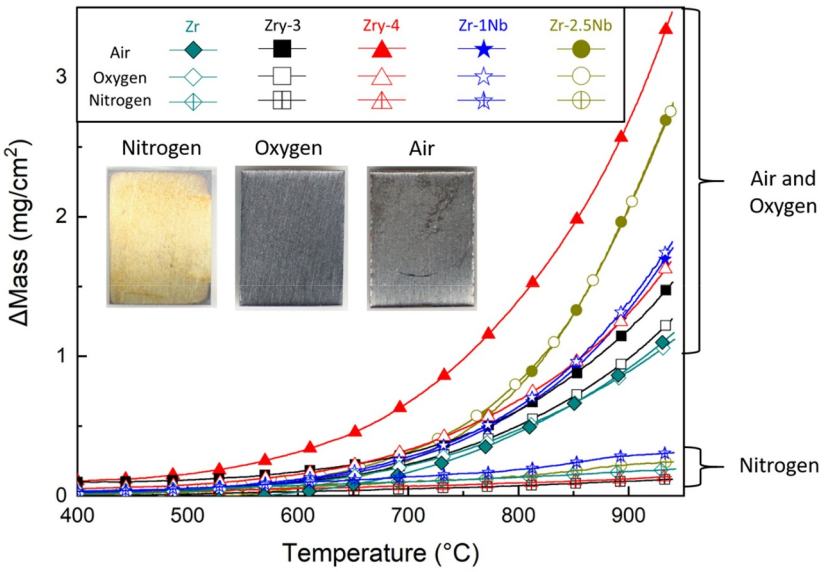

Fig. 3. Non-isothermal mass gain of pure Zr, Zry-3, Zry-4, Zr-1Nb, and Zr-2.5Nb in synthetic air, oxygen, and nitrogen. Samples were heated to 940 °C at 20 $^{°C}/_{min}$. Inset shows macro-images of the surface of the Zry-4 after non-isothermal oxidation.

2.2. Oxidation experiments

All oxidation experiments were performed in a NETZSCH STA-449 F3 Jupiter with thermogravimetric analysis (TGA). The 20-hour isothermal and non-isothermal experiments were completed in two different oxidizing atmospheres: 80% N_2+O_2 (air) or 80% $Ar+O_2$ (oxygen). A custom notched alumina crucible was used to hold the plate sample upright in the furnace, maximizing the surface exposed to the experimental gas while minimizing the contact between the sample and the crucible, as shown in Fig. 2.

During the non-isothermal oxidation experiments, specimens were individually heated to 940 °C at a rate of 20 $^{°C}/_{min}$, held for 10 min to allow the temperature to equilibrate, and cooled back down to room temperature at 20 $^{°C}/_{min}$.

The 20-hour isothermal oxidation measurements were collected at temperatures ranging from 400–800 °C. Specimens were individually heated to the temperature of interest at 20 $^{°C}/_{min}$ with 100 $^{mL}/_{min}$ of ultra-high purity (UHP) argon cleaned with a thermal oxygen getter (OG). After reaching the setpoint temperature the oxidizing gas (either air or oxygen) flowed at 100 $^{mL}/_{min}$ for 20 h. The specimen was then cooled to room temperature in 100 $^{mL}/_{min}$ of UHP-OG argon at 20 $^{°C}/_{min}$.

2.3. Post test characterization

After oxidation, macro images were taken of each sample. The samples were then sectioned with a slow speed saw, mounted in epoxy, polished to 1 μm in a diamond slurry, and imaged with optical microscopy. The cross section of each sample was used to measure oxide thickness every 100 μm, resulting in approximately 80 measurements per sample, which were used to calculate average oxide thickness and associated standard deviation.

To quantify the onset of the breakaway transition, tangent lines were fit to the mass gain data before and after the transition from parabolic to linear kinetics. The intersection of the two lines was considered the breakaway time at each temperature. The mass gain data was normalized to the initial sample surface area and used to assess the oxidation kinetics and determine the activation energy of each sample before and after breakaway.

3. Results

3.1. Oxidation behavior

The results of the normalized non-isothermal thermogravimetric data are summarized in Fig. 3. Experiments done in pure nitrogen resulted in minimal mass gain consistent with the findings of Steinbrück et al. [6]. Samples heated in oxidizing conditions start experiencing rapid mass gain between 500–700 °C. It is interesting to note that the zirconium alloys with Sn and Fe (Zry-3, Zry-4) oxidize much faster in air than in oxygen, whereas this dependence on atmosphere is much less pronounced in pure Zr and zirconium alloys with Nb (Zr-1Nb, Zr-2.5Nb).

The 20-hour isothermal (400–800 °C) oxidation results are summarized in Fig. 4. The *y*-axis scales vary to best display the data. All the zirconium alloys undergo breakaway during oxidation above 700 °C, whereas pure Zr experiences minimal oxidation up to 800 °C. The Zr-2.5Nb oxidizes the most readily of all the materials at 600 and 700 °C up to 20 h. However at 800 °C, as seen in the inset of Fig. 4, Zry-4 experiences breakaway almost immediately during oxidation in air which results in rapid oxidation. The difference between extent of oxidation in air and oxygen containing gases is minimal from 400–700 °C but increases dramatically at 800 °C for all alloys with largest deviations associated with the Sn and Fe based zirconium alloys, which is consistent with the non-isothermal behavior. In addition, Zr-1Nb and Zr-2.5Nb both begin to spall heavily during oxidation at 800 °C in air. An important observation is that the accelerated corrosion effect of nitrogen containing air is most pronounced after breakaway for all materials tested in this study.

Macro images of specimens after 20-hour isothermal oxidation at 600, 700 and 800 °C are shown in Fig. 5. Cross-section images of Zry-4 after isothermal oxidation at 600 and 800 °C in air and oxygen are presented in Fig. 6 to show the change in the oxide before and after the breakaway transition. From these images it seen that before samples undergo breakaway (<700 °C for most alloys in this study), a dark and cohesive oxide is present. After breakaway, a thicker and non-protective oxide is present. In Zry-3 and Zry-4 the post-breakaway oxide has an orange color, while the post-breakaway oxide formed on the Nb alloys is primarily white (although a slight orange tint was observed on the corners and edges after 800 °C oxidation). The Sn–Fe based alloys develop post-breakaway oxide first on the corners and edges as well as

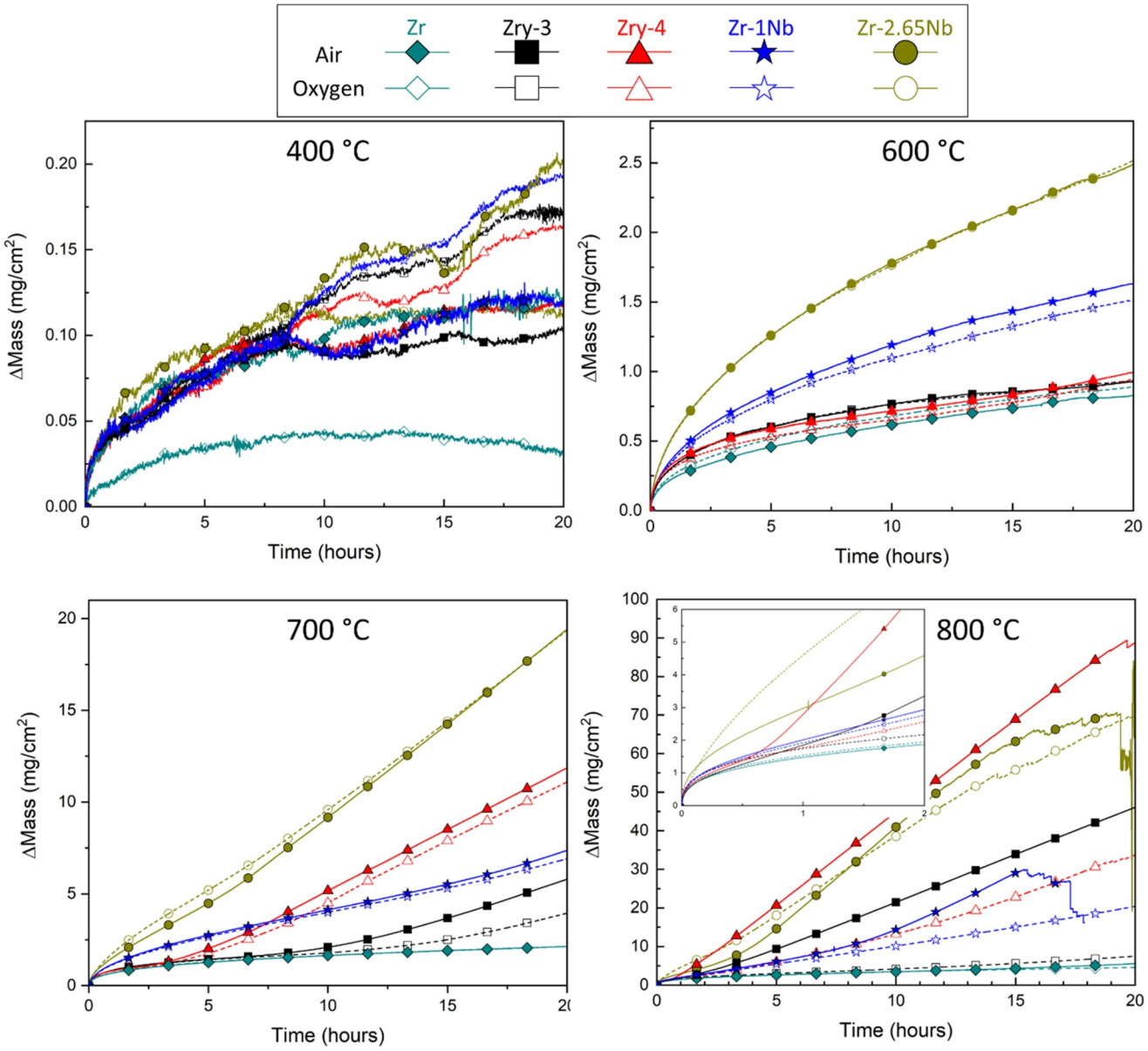

Fig. 4. Normalized mass gain versus isothermal oxidation time of Zr, Zry-3, Zry-4, Zr-1Nb, and Zr-2.5Nb in air and oxygen at 400–800 °C. The inset in the 800 °C graph is the first two hours of the isothermal oxidation showing the onset of breakaway in Zry-3, Zry-4, and Zr-2.5Nb.

isolated nodules on the surface of the samples. The Nb alloys form a network of horizontal cracks on the surface, inside of which the white post-breakaway oxide forms. The effect of nitrogen on the oxidation behavior of the zirconium alloys is seen most clearly after oxidation at 800 °C: oxidation in air results in a cracked oxide, while the oxide formed in oxygen remains comparatively cohesive. After oxidation at temperatures higher than 600 °C, Zr-1Nb becomes mechanically deformed; which is likely attributed to these samples being thinner than the other alloys. During oxidation at 800 °C in oxygen, Zr-1Nb becomes severely mechanically deformed and, in air, most of the sample has oxidized and spalled off. Additionally, an artifact of the positioning of the sample in the crucible is apparent in the Zr and Zry-3 specimens during oxidation at 800 °C, as seen in the upper right side of Fig. 5 where an outline of the crucible is seen corresponding to reduced oxide growth.

The breakaway transition time and the oxide thickness of each alloy after 20 h of isothermal oxidation are summarized in Table 2. As discussed with Fig. 4, breakaway occurs more rapidly in samples oxidized in air compared to those oxidized in oxygen in all cases (except Zr-1Nb at 700 °C and Zr-2.5Nb at 800 °C where breakaway occurs only slightly sooner in oxygen). Additionally, as expected, the oxide formed in air is thicker than that formed in oxygen after breakaway (most notably for Zry-3, Zry-4, and Zr-1Nb). This is best illustrated in Fig. 7, which shows oxide thickness versus isothermal oxidation temperature after 20 h. The difference in oxide thickness between oxidation in air or oxygen continues to increase rapidly with increasing oxidation temperature. However, it should be noted that the deviation associated with the oxide thickness measurements for samples that had reached breakaway was relatively high compared to those that had not reached breakaway due to the cracked nature of the oxide.

4. Discussion

4.1. Oxidation kinetics

The oxidation rate is related to the normalized mass gained during oxidation by the equation [12]:

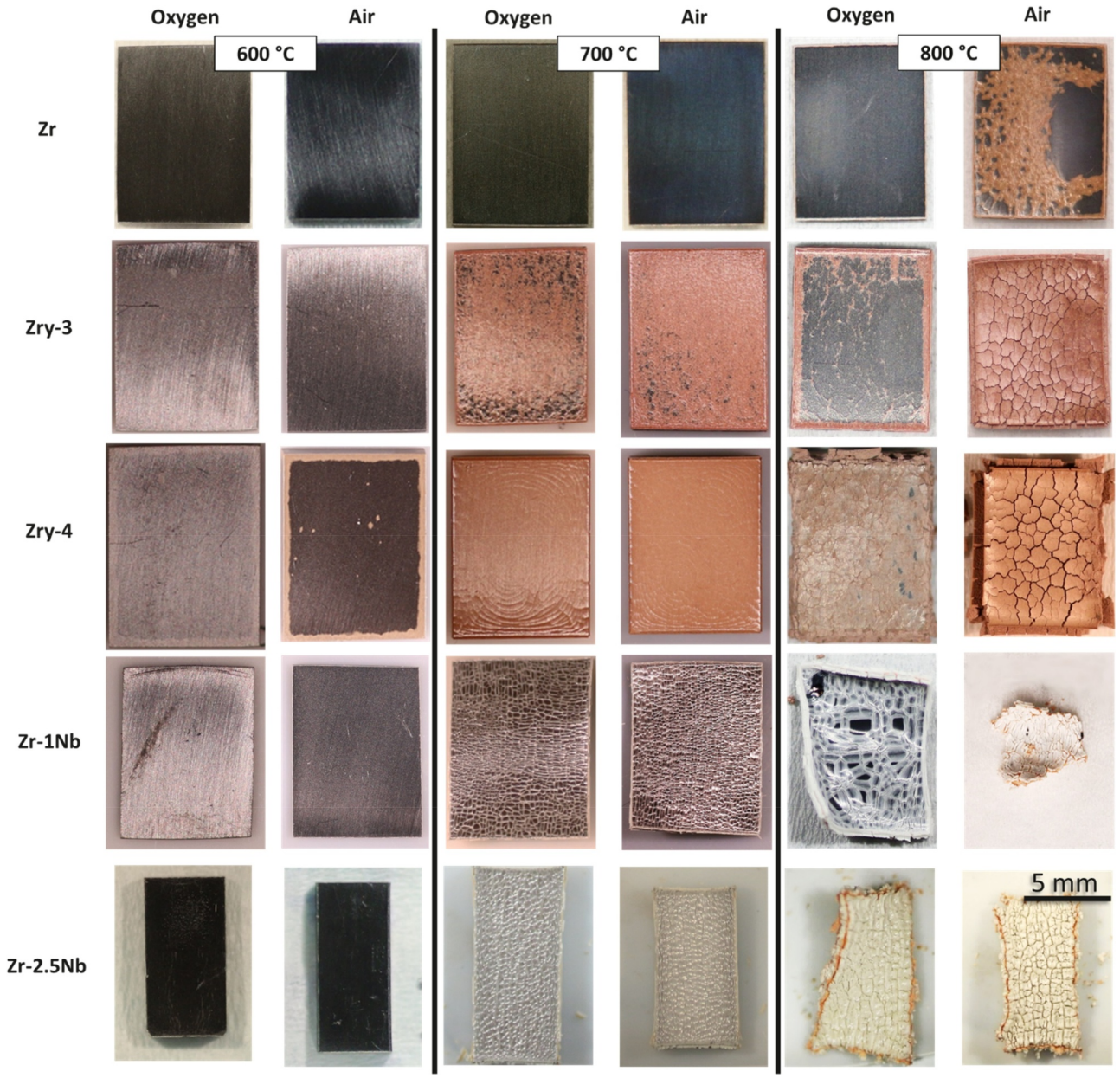

Fig. 5. Macro images of the surface of each alloy showing the material degradation after 20-hour isothermal oxidation at 600, 700, and 800 °C in air and oxygen.

$$W^n = K^*t \left[\frac{kg}{m^2}\right]^n \quad (1)$$

where W is the normalized mass gain, K is the oxidation rate constant, t is oxidation time, and n is the rate law identifier (i.e. $n = 1$ for linear $n = 2$ for parabolic oxidation behavior). The oxidation rate constant is determined for each alloy and isothermal temperature by fitting Eq. (1) to the data in Fig. 4. The pre- and post-breakaway rate constants were determined separately, with pre-breakaway following parabolic ($n = 2$) oxidation behavior and post-breakaway following linear ($n = 1$) oxidation behavior. The activation energy of each alloy before and after breakaway is then determined via an Arrhenius equation according to:

$$\ln(K) = \ln(A) + \left(\frac{1}{T}\right)\left(\frac{-E_a}{R}\right)\left[\frac{J}{mol}\right] \quad (2)$$

where A is a constant, E_a is the activation energy, R is the ideal gas constant, and T is the isothermal oxidation temperature. The $\ln(K)$ values obtained from Eq. (1) are plotted against $^1/_T$ and are fit with a linear trend line. These plots before and after breakaway from oxidation in oxygen are shown in Fig. 8 and the values found for Eq. (2) are listed in Table 3. Activation energy before and after breakaway are obtained from the slopes of these plots and listed in Table 4.

4.1.1. Pre-breakaway

As previously mentioned, the oxidation of zirconium alloys typically follows parabolic or sub-parabolic kinetics until a transition (breakaway) occurs after which the kinetics become linear. After the initial adsorption of oxygen onto the surface of the metal, the parabolic (pre-breakaway) regime is controlled by the diffusion of oxygen anions through the oxide layer [12]. It is suggested in literature that the pre-breakaway oxidation mechanism is such that oxygen anions diffuse inward along crystallite boundaries in the oxide [9]. An inert marker experiment was performed on pure zirconium as well as all four alloys to determine if the same diffusion mechanism applies for all the materials investigated. A thin (50 μm diameter) gold wire was welded onto the surfaces of the samples prior to oxidation at 700 °C in air and in oxygen for 140 min. Similar to literature, these experiments also

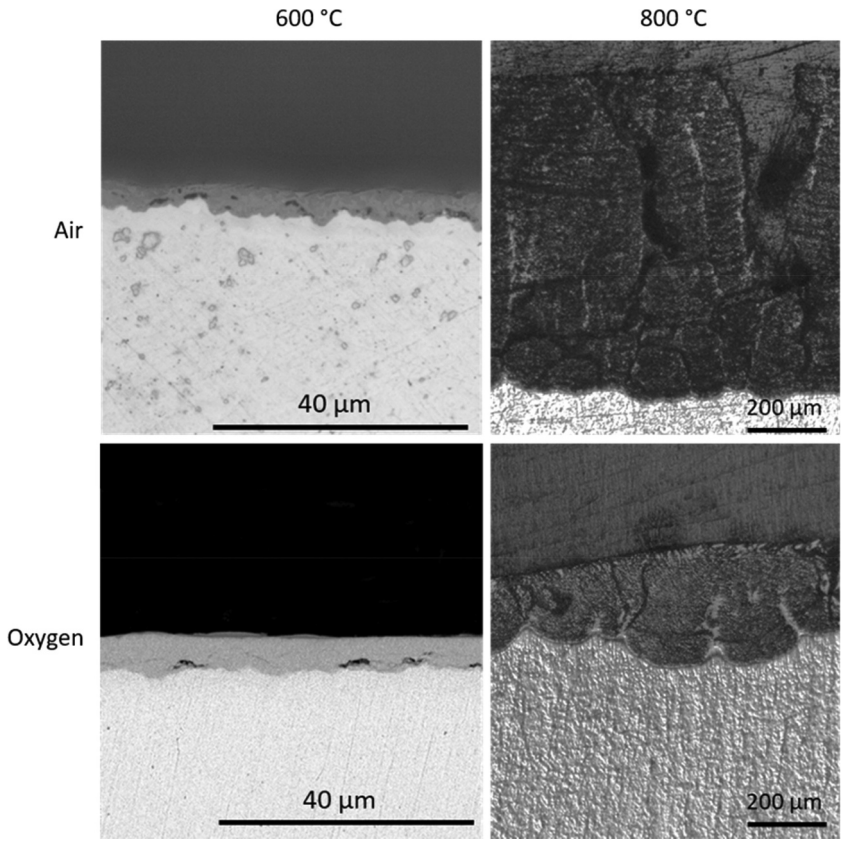

Fig. 6. Representative sample cross-sections after oxidation. The specimen shown is Zry-4 after oxidation in air and oxygen at 600 °C and 800 °C.

Table 2
Time to breakaway determined from isothermal oxidation experiments (Fig. 4) and oxide thickness of pure zirconium, Zry-3, Zry-4, Zr-1Nb, and Zr-2.5Nb after 20-hour isothermal oxidation in air and oxygen environments.

Temp (°C)	Alloy	Air		Oxygen	
		Breakaway onset (hours)	Oxide thickness ± st. dev. (µm)	breakaway onset (hours)	Oxide thickness ± st. dev. (µm)
600	Zr	–	4 ± 1	–	3 ± 1
	Zry-3	–	3 ± 1	–	4 ± 1
	Zry-4	16	4 ± 2	13.5	7 ± 3
	Zr-1Nb	–	8 ± 1	–	8 ± 1
	Zr-2.5Nb	–	17 ± 3	–	12 ± 2
700	Zr	–	10 ± 1	–	12 ± 1
	Zry-3	11.5	30 ± 10	15	20 ± 9
	Zry-4	4.5	80 ± 17	6	70 ± 17
	Zr-1Nb	16.5	30 ± 13	16	30 ± 13
	Zr-2.5Nb	6	105 ± 11	7	50 ± 7
800	Zr	–	60 ± 29	–	17 ± 1
	Zry-3	3	340 ± 28	14.5	30 ± 22
	Zry-4	1.5	790 ± 34	4	20 ± 6
	Zr-1Nb	9.5	190 ± 21	–	60 ± 24
	Zr-2.5Nb	4.5	340 ± 148	4	380 ± 41

suggested that an inward diffusion mechanism is present since the gold wire was found at the oxide/atmosphere interface in all cases. Although more studies would need to be done to confirm the exact oxidation mechanism, it is useful to know that the mechanism appears to agree with literature for all materials investigated.

The rate constants were determined by fitting the pre-breakaway regime with a parabolic fit, neglecting the initial oxidation of the bare metal (initial linear region of mass gain plot). The fitting parameters calculated by the method described in Section 4.1 are listed in Table 3 along with the R^2 value that describes the variance between the data and the fit. For all materials except for Zry-4, there are only two temperatures where a post-breakaway oxidation rate can be extrapolated. For these alloys, an R^2 value of 1 was found, indicating a perfect fit. This is an artifact of fitting two data points, thus the R^2 values are not

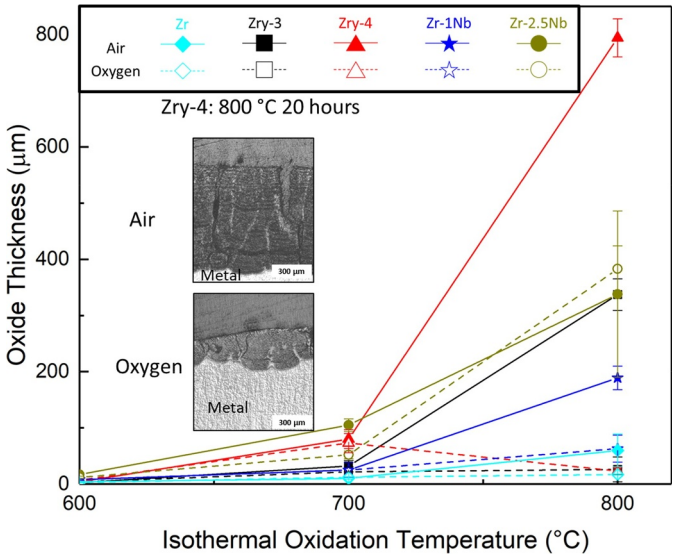

Fig. 7. Average measured oxide thickness versus isothermal oxidation temperature in air and oxygen for all cladding materials. The error increases with increasing oxidation temperature due to the cracked nature of the oxide. The inset shows cross-section images of Zry-4 after 20 h of isothermal oxidation at 800 °C.

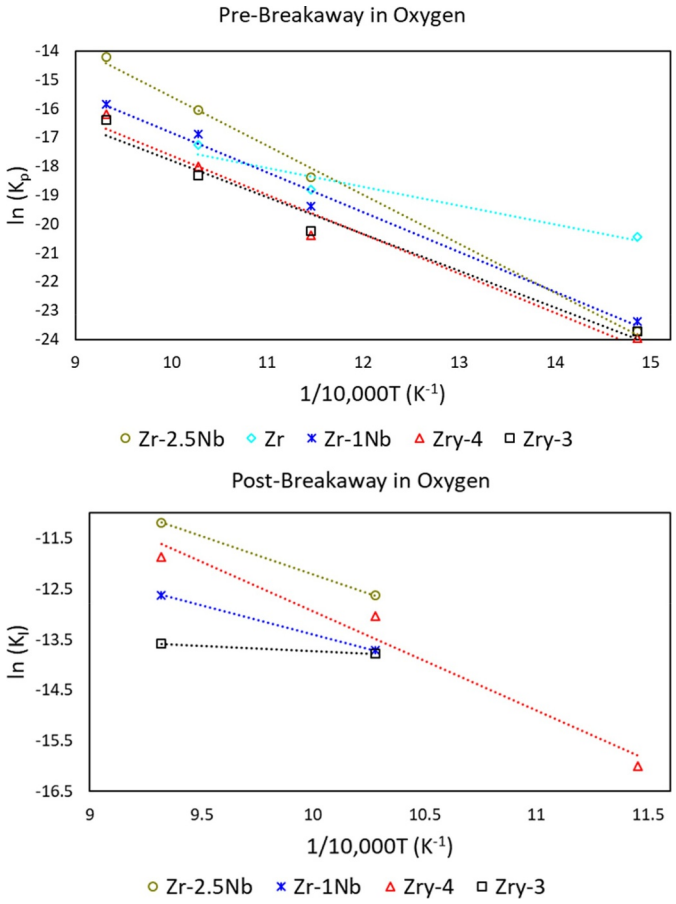

Fig. 8. Arrhenius dependence of oxidation rate constant as a function of temperature after isothermal oxidation in oxygen where K_p and K_l are the parabolic and linear rate constants, respectively. The activation energy for oxidation can be derived from the slope of the plot according to Eq. (2).

reported. The calculated activation energies are plotted with values reported in literature in Fig. 9. The pre-breakaway activation energies are similar between the two atmospheres (within approximately 20 $^{kJ}/_{mol}$) for each alloy, further indicating that the presence of nitrogen in the oxidizing atmosphere does not significantly affect the pre-breakaway oxidation regime. Additionally, the activation energies are similar to values reported in literature. Discrepancies between literature values can be attributed to the wide variety of sample geometry, experimental setup, and oxidizing atmosphere reported.

4.1.2. Post-breakaway

The cracks formed during breakaway (Fig. 6) result in a direct path for oxygen to reach the metal surface, which has been shown to lead to accelerated oxidation kinetics. This transition is intensified by the presence of nitrogen in the atmosphere (Fig. 4 and Table 2). It has been reported in literature that as oxygen is consumed within the cracks of the zirconium oxide, a nitrogen rich phase is formed [12,15]. As the oxygen is refreshed, the ZrN is oxidized in a rapid exothermic reaction, which results in a volume increase and a porous, non-protective oxide [7,12,15]. This post-breakaway regime is best characterized with a linear rate law, where $n = 1$ in Eq. (1). The calculated activation energies for each material in the post-breakaway regime are listed in Table 4 where it is seen that the activation energies for oxidation in air are significantly higher than in oxygen.

5. Conclusion

The oxidation behavior of Zr, Zry-3, Zry-4, Zr-1Nb, and Zr-2.5Nb of similar geometry in 80%$N_2 + O_2$ (air) and 80%$Ar + O_2$ (oxygen) in the temperature range 400–800 °C has been investigated and compared using thermogravimetric analysis. It has been observed that all four alloys exhibit the characteristic kinetic transition from parabolic to linear (breakaway) within 20 h during isothermal oxidation at 700 and 800 °C. In all four alloys, the oxidation behavior is similar to what has been shown in literature; a dense protective oxide forms during pre-breakaway oxidation while the post-breakaway oxide is much thicker, cracked, and less protective [9–11].

Zr-2.5Nb was found to have most rapid oxidation kinetics of all the materials that were investigated and has similar oxidation rates in both air and oxygen. Zry-3 and Zr-1Nb were the most resistant to breakaway and had the slowest oxidation kinetics after breakaway. Zry-3, Zry-4, and Zr-1Nb had faster oxidation kinetics and thicker, more porous oxides after oxidation in air when compared to oxidation in oxygen. The Sn and Fe containing alloys were more sensitive to the oxidizing atmosphere than the Nb containing alloys and exhibited faster oxidation kinetics in air than in oxygen. The inert marker experiment confirmed that for all materials (including pure zirconium), the diffusing species is likely oxygen anions diffusing through the oxide to the underlying metal.

Declarations of interest

None.

Data availability

The raw data required to reproduce these findings are available to download from Mendeley Data. The processed data required to reproduce these findings are available to download from Mendeley Data.

Table 3
Constants and slopes obtained from Arrhenius fits (Eq. (2)) as described above. The Arrhenius dependence for zirconium and zirconium alloys before and after breakaway during isothermal oxidation in oxygen is shown in Fig. 8.

	Pre-breakaway						Post-breakaway					
	Air			Oxygen			Air			Oxygen		
	ln(*A*)	E_a/R (K)	R^2	ln(*A*)	E_a/R (K)	R^2	ln(*A*)	E_a/R (K)	R^2	ln(*A*)	E_a/R (K)	R^2
Zr	−5.30	−12,890	0.98	−3.36	−14,954	0.99	Does not occur					
Zry-3	−2.88	−14,535	0.98	−5.05	−12,744	0.97	5.74	−18,719	–	−11.6810	−2041.8	–
Zry-4	−3.26	−14,018	0.95	−3.98	−13,636	0.97	21.54	−34,459	0.96	6.6628	−19,612	0.97
Zr-1Nb	−1.97	−14,821	0.99	−3.07	−13,769	0.99	7.96	−20,897	–	−1.9614	−11,441	–
Zr-2.5Nb	−0.69	−15,384	0.99	1.46	−17,029	0.99	4.97	−17,087	–	2.7596	−14,972	–

Table 4
Calculated activation energies (E_a) of each alloy in air or oxygen compared to values reported in literature. Activation energies are calculated for pre-breakaway and post-breakaway regimes.

	Air			Oxygen		
	Pre-breakaway E_a ($^{kJ}/_{mol}$)	Literature pre-breakaway E_a ($^{kJ}/_{mol}$)	Post-breakaway E_a ($^{kJ}/_{mol}$)	Pre-breakaway E_a ($^{kJ}/_{mol}$)	Literature pre-breakaway E_a ($^{kJ}/_{mol}$)	Post-breakaway E_a ($^{kJ}/_{mol}$)
Zr	107	–	Does not occur	124	Porte et al. [16]: 179 Charles [17]: 159	Does not occur
Zry-3	121	–	156	106	–	17.0
Zry-4	117	Steinbrük and Böttcher [5]: 86.8 Duriez et al. [3]: 89.4 Benjamin et al. [18]: 114 Coindreau et al. [19]: 190 Powers et al. [20]: 130	286	113	Steinbrük and Schaffer [7]: 45.2	163
Zr-1Nb	123	Steinbrük and Böttcher [5]: 65.6 Duriez et al. [3]: 54.2	174	114	–	95.0
Zr-2.5Nb	128	Hobbs et al. [21]: 79.4 Arima et al. [22]: 150	142	142	–	124

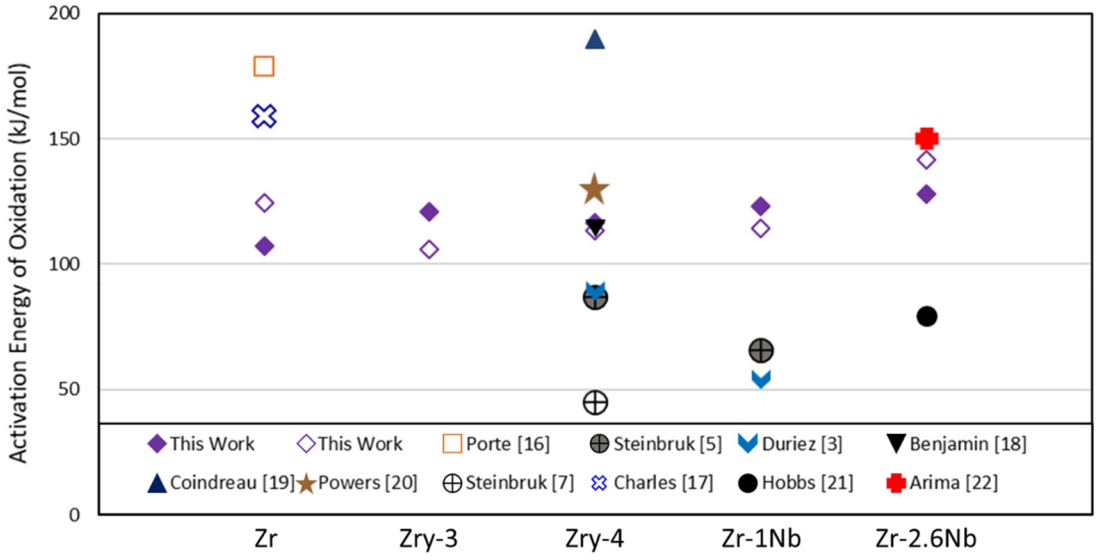

Fig. 9. Calculated pre-breakaway activation energies for Zr, Zry-3, Zry-4, Zr-1Nb, and Zr-2.5Nb compared to reported values. Solid symbols represent values obtained from oxidation in air, hollow symbols represent values obtained from oxidation in oxygen.

Acknowledgments

The work reported here was funded primarily through Department of Energy's National Nuclear Security Administration (DOE-NNSA) Office of Materials Minimization and Management. The authors would like to acknowledge K. Lester, L. Monteiro, N. Blancett, Y. Rodriguez-Ortego, and S. Mekonen at Boise State University for assistance in preparing and imaging samples. The authors would also like to acknowledge P. Boysen in the BSU machine shop for machining the sample coupons from the original sheet. Additionally, thanks to G. Alanko at ATI Specialty Alloys and Components for providing the Zr-2.5Nb material.

References

[1] J. Carmack, Future transient testing of advanced fuels (INL/EXT-09-163920), United States, 2009.

[2] C. Duriez, D. Drouan, G. Pouzadoux, Reaction in air and in nitrogen of pre-oxidised zircaloy-4 and M5™ claddings, J. Nucl. Mater. 441 (2013) 84–95, https://doi.org/10.1016/j.jnucmat.2013.04.095.

[3] C. Duriez, T. Dupont, B. Schmet, F. Enoch, Zircaloy-4 and M5® high temperature oxidation and nitriding in air, J. Nucl. Mater. 380 (2008) 30–45, https://doi.org/10.1016/j.jnucmat.2008.07.002.

[4] M. Lasserre, V. Peres, M. Pijolat, O. Coindreau, C. Duriez, J.P. Mardon, Qualitative analysis of Zircaloy-4 cladding air degradation in O_2-N_2 mixtures at high temperature, Mater. Corros. 65 (2014) 250–259.

[5] M. Steinbrück, M. Böttcher, Air oxidation of Zircaloy-4, M5® and ZIRLO™ cladding alloys at high temperatures, J. Nucl. Mater. 414 (2011) 276–285, https://doi.org/10.1016/j.jnucmat.2011.04.012.

[6] M. Steinbrück, Prototypical experiments relating to air oxidation of Zircaloy-4 at high temperatures, J. Nucl. Mater. 392 (2009) 531–544, https://doi.org/10.1016/j.jnucmat.2009.04.018.

[7] M. Steinbrück, S. Schaffer, High-temperature oxidation of Zircaloy-4 in oxygen-nitrogen mixtures, Oxid. Met. 85 (2016) 245–262, https://doi.org/10.1007/s11085-015-9572-1.

[8] E.T. Hayes, A.H. Roberson, Some effects of heating zirconium in air, oxygen, and nitrogen, J. Electrochem. Soc. 96 (1949) 142–151.

[9] B. Cox, V.G. Kristsky, C. Lemaignan, V. Polley, I.G. Ritchie, H. Ruhmann, V.N. Shishov, Waterside corrosion of zirconium alloys in nuclear power plants, Vienna, Austria, 1998.

[10] M. Lasserre, V. Peres, M. Pijolat, O. Coindreau, C. Duriez, J.P. Mardon, Modelling of Zircaloy-4 accelerated degradation kinetics in nitrogen–oxygen mixtures at 850 °C, J. Nucl. Mater. 462 (2015) 221–229, https://doi.org/10.1016/j.jnucmat.2015.03.052.

[11] M. Lasserre, O. Coindreau, M. Mermoux, M. Pijolat, V. Peres, J.P. Mardon, Study of Zircaloy-4 cladding air degradation at high temperature, Proceedings of the International Conference Nuclear Engineering ICONE21-16440, 2013, pp. 1–9.

[12] E. Beuzet, J.S. Lamy, A. Bretault, E. Simoni, Modelling of Zry-4 cladding oxidation by air, under severe accident conditions using the MAAP4 code, Nucl. Eng. Des. 241 (2011) 1217–1224, https://doi.org/10.1016/j.nucengdes.2010.04.024.

[13] B. Cox, Some thoughts on the mechanisms of in-reactor corrosion of zirconium alloys, J. Nucl. Mater. 336 (2005) 331–368, https://doi.org/10.1016/j.jnucmat.2004.09.029.

[14] C. Duriez, M. Steinbrück, D. Ohai, T. Meleg, J. Birchley, T. Haste, Separate-effect tests on zirconium cladding degradation in air ingress situations, Nucl. Eng. Des. 239 (2009) 244–253, https://doi.org/10.1016/j.nucengdes.2008.10.017.

[15] J. Stuckert, Z. Hózer, A. Kiselev, M. Steinbrück, Cladding oxidation during air ingress. Part I: experiments on air ingress, Ann. Nucl. Energy. 93 (2016) 4–17, https://doi.org/10.1016/j.anucene.2015.12.034.

[16] H.A. Porte, J.G. Schnizlein, R.C. Vogel, D.F. Fischer, Oxidation of zirconium and zirconium alloys, J. Electrochem. Soc. 107 (1960) 506, https://doi.org/10.1149/1.2427733.

[17] R.G. Charles, Prolonged oxidation of zirconium at 350° and 450 °C, Trans. Am. Inst. Min. Metall. Eng. 212 (1958) 101.

[18] A. Benjamin, D.J. McCloskey, D.A. Powers, S. Dupree, Spent fuel heatup following loss of water during storage, Nucl. Technol. 49 (1980) 274–294.

[19] O. Coindreau, C. Duriez, S. Ederli, Air oxidation of Zircaloy-4 in the 600–1000 °C temperature range: modeling for ASTEC code application, J. Nucl. Mater. 405 (2010) 207–215, https://doi.org/10.1016/j.jnucmat.2010.07.038.

[20] D.A. Powers, L.N. Kmetyk, R.C. Schmidt, A Review of the Technical Issues of Air Ingression During Severe Reactor Accidents, Nuclear Regulatory Commission, Washington, DC (United states). Div. of Systems Research; Sandia National Labs, Albuquerque, NM (United States), 1994.

[21] L.W. Hobbs, V.B. Rosen, S.P. Mangin, M. Treska, G. Hunter, Oxidation microstructures and interfaces in the oxidized zirconium knee, Int. J. Appl. Ceram. Technol. 2 (2005) 221–246, https://doi.org/10.1111/j.1744-7402.2005.02025.x.

[22] T. Arima, K. Miyata, K. Idemitsu, Y. Inagaki, Oxidation properties of Zr–Nb alloys at 973–1273 K in air, Prog. Nucl. Energy. 51 (2009) 307–312, https://doi.org/10.1016/j.pnucene.2008.08.001.